Self-assembled anti-reflection coatings for light trapping based on SiGe random metasurfaces

Mohammed Bouabdellaoui,[1,2], Simona Checcucci,[1,3,4,†] Thomas Wood,[1,‡,*] Meher Naffouti,[1,5,**], Robert Paria Sena,[1] Kailang Liu,[1] Carmen M. Ruiz,[1] David Duche,[1] Judikael le Rouzo,[1] Ludovic Escoubas,[1] Gerard Berginc,[6] Nicolas Bonod,[7] Mimoun Zazoui,[2] Luc Favre,[1] Leo Metayer,[1] Antoine Ronda,[1] Isabelle Berbezier,[1] David Grosso,[1] Massimo Gurioli,[1] and Marco Abbarchi*[1]

[1] *CNRS, Aix-Marseille Université, Centrale Marseille, IM2NP, UMR 7334, Campus de St. Jérôme, 13397 Marseille, France*

[2] *Laboratory of Physics of Condensed Matter and Renewable Energy, Faculty of Sciences and Technology, Hassan II University of Casablanca, 146 Mohammedia, Morocco*

[3] *European Laboratory for Nonlinear Spectroscopy (LENS), 50019 Sesto Fiorentino, Italy*

[4] *Dipartimento di Fisica ed Astronomia, Universitá degli Studi di Firenze, 50019 Sesto Fiorentino, Italy*

[5] *Laboratoire de Micro-optoélectronique et Nanostructures Faculté des Sciences de Monastir Université de Monastir 5019 Monastir, Tunisia*

[6] *Thales Optronics, Elancourt, France*

[7] *Aix-Marseille Université, CNRS, Centrale Marseille, Institut Fresnel, Marseille, France*

(Dated: January 25, 2018)

We demonstrate a simple self-assembly method based on solid state dewetting of ultra-thin silicon films and germanium deposition for the fabrication of efficient anti reflection coatings on silicon for light trapping. Via solid state dewetting of ultra-thin silicon on insulator and epitaxial deposition of Ge we fabricate SiGe islands with a high surface density, randomly positioned and broadly varied in size. This allows to reduce the reflectance to low values in a broad spectral range (from 500 nm to 2500 nm) and a broad angle (up to 55 degrees) and to trap within the wafer a large portion of the impinging light ($\sim$40%) also below the band-gap, where the Si substrate is non-absorbing. Theoretical simulations agree with the experimental results showing that the efficient light coupling into the substrate mediated by Mie resonances formed within the SiGe islands. This lithography-free method can be implemented on arbitrarily thick or thin SiO_2 layers and its duration only depends on the sample thickness and on the annealing temperature.

I. INTRODUCTION

Efficient anti-reflection coatings (AR) have been intensively studied with many different approaches having been explored for this purpose[1–3], such as multi-layered thin-films[4,5], graded index matching via surface texturing with micro- and nano-structures[6–11], plasmonic metasurfaces[12–14] and more recently, metasurfaces[15–21] based on ordered arrays of sub-micrometric dielectric antennas (dielectric Mie resonators[22–28]). Depending on the application of the AR different aspects (lowest value of the total reflectance, broad spectral range, broad acceptance angle, transparency or light trapping) determine the optimal features and fabrication method.

A convenient and efficient solution for enhancing light absorption relies on the exploitation of disordered structures[13,29–33]. The superior AR properties of disordered systems account for the importance of this approach with respect to its ordered counterparts and it has been recently proposed[20] and implemented[19] using dielectric Mie resonators. Such results, obtained via *top-down* methods,[19] demonstrate that combining disorder and Mie resonators provides efficient AR coatings at visible frequencies. However, the ease of fabrication at affordable prices on reasonable timescales, are major requirements for realistic devices implemented on large scales and conventional *top-down* fabrication processes are unable to meet such criteria.

Random metasurfaces offer the basis for the development of less costly and large-scale bottom-up fabrication methods based on self-assembly. One viable and promising route is solid-state dewetting of ultra-thin films of metals[18,34–41] and semiconductors,[42–46] a natural phenomenon exploited for the self-assembly of high-quality photonic structures. The instability giving rise to the dewetting phenomenon in thin films is mediated by the surface diffusion of atoms and occurs upon annealing at high temperature (even well below the melting point of the material)[47–58]. Arrays of well separated islands, featuring a random spatial organization and a relatively large spread of sizes and shapes can be produces. The potential of this method in semiconductors has not been completely exploited and, for example, AR coatings formed by self-assembly have not yet been reported. In fact, one of the main limits of this method is the relatively low density of the dewetted particles: in solid state dewetting, as in other self-assembly methods for 3D nanostructures (e.g. Stranski Krastanov growth in IV-IV and III-V compounds) a linear dependence links the initial thickness of the Si(Ge) layer and the final size (and density) of the dewetted islands[59]. This feature naturally leads to large inter-particle distances and limits the exploitation of dewetting for nanophotonics.

In this work, we report on the implementation of a self-assembly method based on dewetting and epitaxial growth for the fabrication of AR coatings. We manage to overcome the well-known limitations of most common self-assembly processes: the correlation between size and density of the islands. Furthermore, in contrast with previous reports of SiGe dewetting where marked spatial anisotropies affected the size distribution of the islands,[44,60,61] in our samples large and small particles are perfectly mixed, providing a homogeneous arrangement of randomly positioned islands. The epitaxial growth during dewetting represents a step forward towards increasing the density of large particles capable of sustaining Mie reso-

nances.

We demonstrate efficient AR coatings both at visible and near-infrared frequencies, based on Mie resonances from high-density, randomly organized, SiGe-islands. Finite difference time domain simulations (FDTD) highlight the resonant effect leading to the enhanced coupling and light-trapping of the impinging light towards the underlying Si wafer. A systematic and quantitative comparison of our metasurfaces with thin films-based AR based on thin films highlights the superior performance of our approach in enhancing the light coupling within the underlying Si wafer, a useful trait for photovoltaic and detector applications.

Similar approaches in the literature[15] include *ad hoc* Si_3N_4 conformal layers on top of the Mie resonators. In our approach we extend this idea to a double layer of Si_3N_4 and SiO_2 on the islands and on the backside of the samples. Thus, we target specific wavelength ranges optimizing the AR for below band-gap frequencies, where the total reflectance (R_{tot}) reaches 7-20%, and for above band-gap frequencies, where R_{tot} is reduced to few percentages. Angle-resolved measurements confirm that these properties are maintained within an acceptance angle of about $\pm$55 degrees.

We systematically address the different phenomena determining the spectral features of our AR coatings providing a precise discrimination between the main photometric parameters: total reflectance, specular reflectance, total transmission and reflected scattering. We show that in our dielectric metasurfaces (also when covered with conformal layers[15]) the dominant contribution to R_{tot} comes from nearly-isotropic, backscattering whereas that of specular reflectance is only a few per cent of it. Monitoring the total transmission T_{tot} for below band-gap frequencies allows to highlight a relevant light trapping within the substrate (T_{tot} + $R_{tot} < 100\%$).

The paper is organized as follows: in section II we address the main advantages and issues of solid state dewetting as a self-assembly method for Si- and SiGe-based Mie resonators and we provide a description of the built-in morphological and structural properties of the samples under investigation. In section III we provide a deep characterization of the spectroscopic features of the SiGe-based random metasurfaces, addressing the light management in terms of total reflection, total transmission, light trapping, angular and polarization dependent reflection and finally discriminating between reflected scattering and reflected diffusion. We address both cases of bare islands and islands covered with conformal layers of SiO_2 and Si_3N_4 providing a theoretical interpretation of the results and a systematic comparison with the performances of conventional flat layers as ARs. In section IV we discuss the relevance of our findings putting them in the context of dielectric ARs based on ordered Mie resonators and in section V we draw the conclusions.

II. METHODS

A. SOLID STATE DEWETTING FOR $SiGe$-BASED MIE RESONATORS

Intrinsic features of solid state dewetting of silicon films are set by the initial thickness of the thin, crystalline layer the period of the underlying Rayleigh-like instability, determining all the built-in structural parameters of the islands, such as their density, size and equilibrium shape[44,50,52,54,62]. All these properties can be modified by adding Ge before, during or after dewetting[42–45,60,61,63] potentially providing full control over their physical properties. However, in SiGe-based samples, Si-rich and Ge-rich particles are spatially separate, leading to large inhomogeneities of the morphological properties over micrometric distances[44,60,61] that make this method unsuitable for performing devices.

A relatively large vertical aspect ratio ($\eta = h/r$, where h is the particle's height and $r = d/2$ is the half of its base size) is necessary for the formation of intense and sharp resonances in dielectric Mie resonators[64]. While η remains low in pure Si islands, it is higher in SiGe Si[45,61]. Here it is worth mentioning that the larger extinction coefficient of Ge with respect to Si at short wavelengths leads to enhanced losses (Supplementary Information SI Fig.SI. 2). However, theoretical simulations[65,66] and practical implementations[45,67,68] have unambiguously demonstrated the relevance of Ge for dielectric Mie resonators, at least for wavelengths larger than $\sim$500 nm.

From this picture it emerges that solid state dewetting of SiGe has a great potential for nanophotonics on large scales being a spontaneous phenomenon, but a convincing demonstration of its performances is still missing. In what follows we show that a modified dewetting protocol allows to overcome the above mentioned limitations, providing a clearcut demonstration of the relevance of this method for the implementation of SiGe-based Mie resonators on large scales.

B. EXPERIMENTAL

In order to overcome the intrinsic features of solid state dewetting of Si (low particles density and small η) we modified the fabrication process by adding a large amount of Ge during the annealing step (300 monolayers MNLs at 800°C, Fig.1 a)). An accurate description of the fabrication process is reported in the SI along with a detailed investigation of SEM, TEM and AFM imaging of the fabricated samples is reported in SI (Fig.SI. 1 and relative discussion). From this structural investigation, we highlight: i) a random formation of the islands and a complete lack of spatial organization (as accounted for by the Fourier transform of a SEM image of sample II in the bottom inset of the central panel of Fig.1 b)); ii) a homogeneous distribution of large and small islands perfectly mixed together eventually showing a bimodal size distribution (Fig.1 b)); iii) a lack of elongation of the islands along preferential crystallographic directions or a more pronounced symmetry for a family of islands[44,60,61]; iv) presence

of dislocations in both families of particles (Fig.SI. 1 f) and g)). All these features are unique of this fabrication procedure and very similar results were obtained with samples grown in slightly different experimental conditions (e.g. at 780 °C) accounting for the robustness of the approach (not shown).

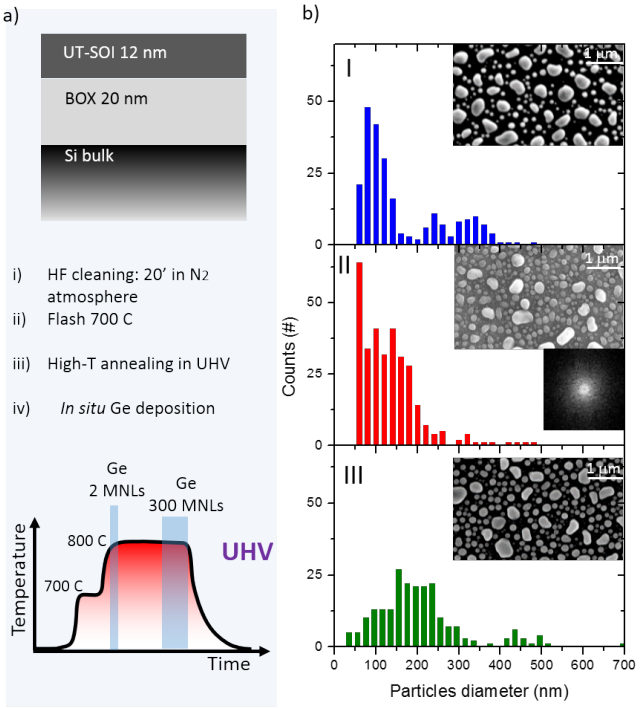


FIG. 1. *Sample fabrication and particles' size distribution*. a) Diagram of the UT-SOI sample composition (12 nm of monocrystalline Si atop 20 nm of buried oxide, BOX) and description of the fabrication steps (i-iv). The bottom part describes the annealing cycle in the ultra-high vacuum (UHV) of the molecular beam reactor and the Ge deposition steps. Additional details of the fabrication process are provided in the Methods section. b) Statistical distribution of particle size for sample I (top panel), II (central panel) and III (bottom panel). The insets show high-resolution SEM images of the dewetted samples. For sample II inset shows also the two-dimensional Fourier transform of a 9×9 μm^2 SEM image.

After dewetting and Ge supply, we deposited conformal layers of SiO_2 and Si_3N_4 on top of the islands as well as on the back face of the samples via plasma enhanced chemical vapor deposition. This step allows the optimization their anti-reflection properties as detailed later. The list of the samples and their features are summarized in Table I.

From AFM images (Fig.SI. 1 c), d) and e)) we highlight rather large geometrical aspect ratios η exceeding 0.7[45,61] of bare SiGe islands and progressive smoothing of the samples' roughness when increasing the thickness of the conformal layers (e.g. the root mean square, RMS goes from ∼58 nm for sample II up to ∼35 nm for sample II-C, Fig.SI. 1 c), d) and e)).

TABLE I. List of samples with corresponding thickness of the SiO_2 and Si_3N_4 layers deposited on top of the SiGe islands (T) and on the backside (B). All the reported thicknesses are expressed in nm.

Sample	T SiO_2	T Si_3N_4	B Si_3N_4	B SiO_2
I	0	0	0	0
I-A	0	130	100	100
I-B	0	100	100	100
I-C	0	70	100	100
II	0	0	0	0
II-A	120	120	80	80
II-B	100	100	80	80
II-C	80	80	80	80
III	0	0	0	0
III-A	0	130	100	100
III-B	0	100	100	100
III-C	0	70	100	100

III. OPTICAL CHARACTERIZATION AND SIMULATIONS

A description of the instruments and methods used for spectroscopy is reported in the devoted section in the SI. The total reflectance R_{tot} of a Si wafer is determined by the refractive index contrast with air, and by its thickness: for frequencies below the Si band-gap, the transparency of the material calls into play the reflection from the backside of the wafer. This determines a sharp increase of R_{tot} at about 1050 nm (Fig.2 a)). This increased value of R_{tot} can be quantified in about 15-20% by simulating the reflection from the top face and from both top and bottom faces of a thick Si slab (respectively thick, purple line and thin, orange line in Fig.2 a)).

The total reflectance R_{tot} for a dewetted 12 nm thick SOI is compared to that of a Si wafer (Fig.2 b)). The small effect of the dewetted sample on the impinging light implies that *per se*, dewetting is not suitable for AR. Samples I, II and III with SiGe island however, show a pronounced AR effect with respect to the bare Si wafer (Fig.2 b)). At frequencies larger than the Si band-gap the value of R_{tot} is about 4-12%, whereas at larger wavelengths, this value rises to about 25-30% due to the transparency of the substrate and the back-face reflection. We observe that samples I and III feature an enhanced light coupling in the substrate at near-infrared frequencies and more pronounced fluctuation of R_{tot} with respect to II, which springs from their particles' larger average size and the more pronounced bimodal size distribution (Fig.1 b)).

While the minimum of R_{tot} for bare SiGe islands is not very low, the most remarkable feature of the AR effect of our metasurface is its extension to all the investigated frequencies with a very smooth spectral dependence. In fact, even if conventional ARs based on thin film coatings can provide lower values of R_{tot} at specific wavelengths, they fail in matching the performances of our AR when considering the full spectrum from visible to near-infrared. These features are systematically investigated in the SI Fig.SI. 6 a), b) and c) where the spectra of simulated interferential ARs based on a SiO_2 single layer, a Si_3N_4 single layer and a SiO_2 on Si_3N_4 double layer are compared with the spectra of samples I, II and

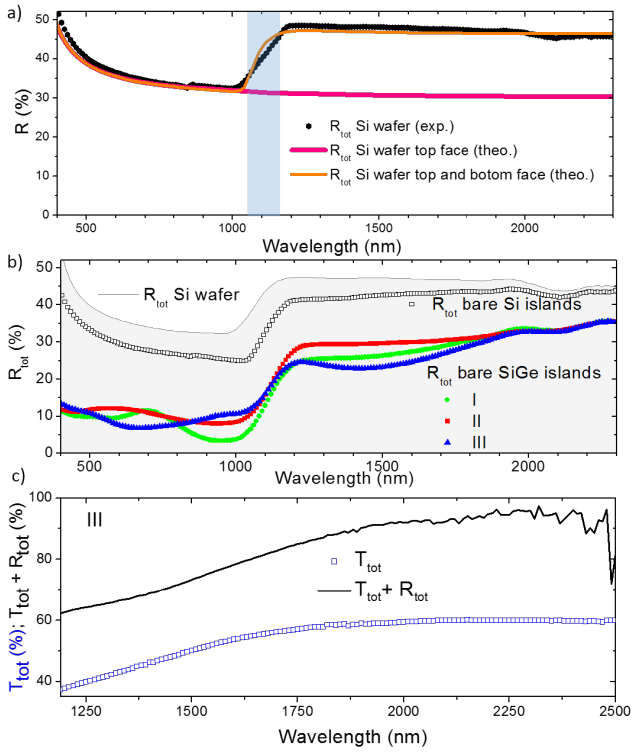


FIG. 2. *Total reflectance R_{tot} for Si- and SiGe-based metasurfaces.* a) R_{tot} in the full investigated spectral range for a Si wafer. Experimental data, black circles; theoretical simulation for the top face only, thick purple line; theoretical simulation for the both top and bottom faces, thin, orange line. The shaded area highlights the transition from above- to below band-gap frequencies. b) Experimental data for R_{tot} measured on: Si wafer (gray line and shaded area), bare Si islands (empty black squares) and bare SiGe islands sample I, II and III (respectively green circles, red squares and blue triangles). c) Total transmission T_{tot} (blue squares) and total transmission plus total reflection T_{tot} + R_{tot} (black line) for samples III. The error in the measured light intensity is less than 2% in at longer wavelengths where the white lamp used for illumination is less intense.

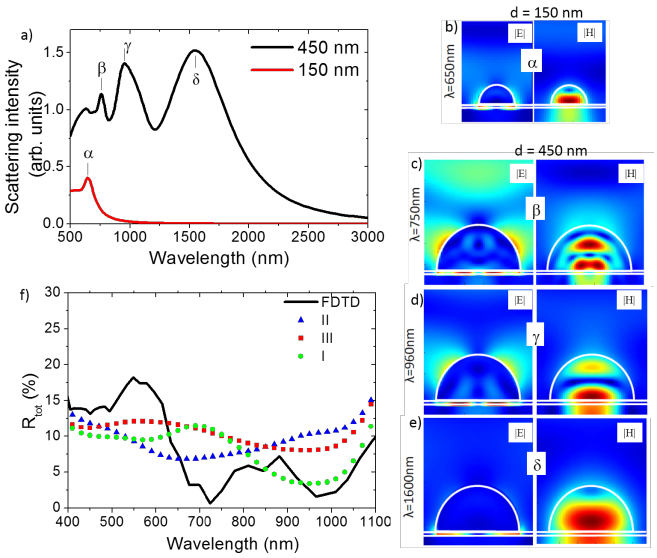


FIG. 3. *FDTD simulations.* a) Scattering intensity of an individual island having base size of 150 nm (vertical aspect ratio 1/2). b) Scattering intensity of an individual island having base size of 450 nm (vertical aspect ratio 1/2). c) Near-field maps of the intensity of the electric field ($|E|$) and magnetic field ($|H|$) at 650 nm for the small particle simulated in a). The white lines highlight the shape of the island and the BOX. d) Near-field maps of the intensity of the electric field and magnetic field at 750 nm for the large particle simulated in b). e) Near-field maps of the intensity of the electric field and magnetic field at 960 nm for the large particle simulated in b). f) Comparison between the measured R_{tot} for samples I, II and III and the FDTD simulation taking into account a random distribution of small (150 nm in diameter) and large (450 nm in diameter) SiGe islands.

III. While the average value of R_{tot} for the best interferential layer is above 26%, the SiGe-based metasurfaces are always below 25% (SI Fig.SI. 6 g), h), i) and j)). A summary of this investigation is shown in table II.

Another relevant parameter necessary for defining the range of uses of a device is its total transmission T_{tot}. Bare SiGe islands exhibit values of T_{tot} between about 35% and 60% in the range 1200 to 2500 nm (Fig.2 c)). By adding to T_{tot} the corresponding value of R_{tot}, we can see that a significant portion of light is not transmitted nor reflected (T_{tot} + R_{tot} < 100%, Fig.2 c)): about 40% of the total at 1200 nm is retained within the wafer (see also the data summarized in table II). We interpret it as a light-trapping phenomenon already reported in similar systems based on dielectric Mie resonators[21]: the presence of 3D resonant scatterers on the sample surface imposes strong modifications to the propagation of the impinging light beam, leading to its partial trapping within the wafer. This feature represents a very important characteristic of our AR and differentiates them from to conventional flat AR where, at these frequencies, T_{tot} + R_{tot} = 100% (not shown) and no light trapping is possible irrespective of the performance in terms of AR (see also table II). Importantly, the possibility to enhance the light absorption could be a valuable tool for extending the quantum efficiency of Si-based light detectors (such as CCD cameras) in this frequency range.

FDTD simulations were used to model the experimental findings (see the dedicated section the SI for details). They were first used to address the scattering intensity of individual small and large islands (respectively diameter d = 150 nm and d = 450 nm). The scattering intensity of small islands feature a sharp peak at ∼650 nm (α, Fig.3 a) and b)). The electric and magnetic field intensity maps at 650 nm, respectively show that $|E|$ is rather confined below the island within the buried oxide (BOX), whereas $|H|$ is well channeled into the substrate (Fig.3 b)). These features are quite similar to what was shown for SiGe islands.[45] However, in the present study the very thin BOX favors a more efficient light coupling within the Si wafer.[15,64] The scattering intensity of large islands exhibit three main peaks in the investigated spectral range (β, γ and δ, Fig.3 a), c), d) and e)). As for the previous case of small islands, the field intensity maps at ∼750 nm, ∼960 nm

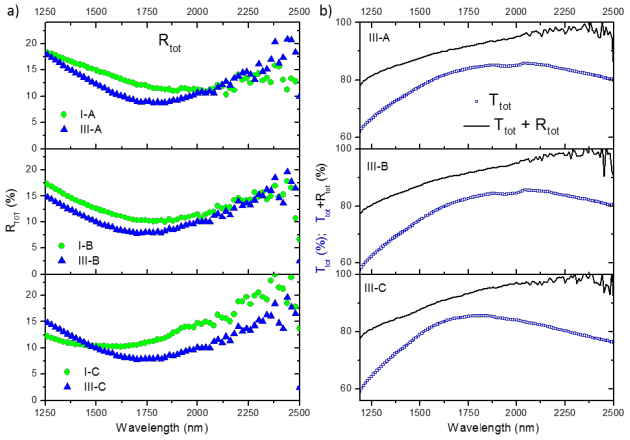


FIG. 4. *Below band-gap anti-reflection coating: samples I-A, -B,-C and III-A, -B and -C* a) From the top to the bottom panel: total reflectance R_{tot} at quasi-normal incidence for samples I-A and III-A, I-B and III-B, and I-C and III-C. b) From the top to the bottom panel: total transmission T_{tot} (blue squares) and T_{tot} + R_{tot} (black line) at quasi-normal incidence for samples III-A, III-B and III-C. The error in the measured light intensity is less than 2% in at longer wavelengths where the white lamp used for illumination is less intense.

and ∼1600 nm, show that $|E|$ is rather confined within the BOX, whereas $|H|$ is well coupled into the substrate. These simulations show that SiGe-based Mie resonators are able to channel light from the ambient in the substrate thanks to the presence of resonantly confined fields extending in the underlying Si wafer. Furthermore, the spread in size and the large density of the particles allows for a broad and smooth light coupling.

Simulations of R_{tot} on randomly distributed resonators of two size-family show rather strong fluctuations between ∼18% and 1% in a spectral interval spanning from ∼400 nm to 1100 nm (black line in Fig.3 f); for R_{tot} we limit our investigation to above band-gap frequencies as the FDTD method does not allow to easily take into account the effect of the backside of the sample. Despite the rough approximations used for describing the particles size distribution in FDTD simulations, the overall agreement with experiments is fairly good (Fig.3 f)). Clearly, the presence of many differently sized particles in experiments smooths the features of R_{tot}, but its average value in simulations and experiments are quite similar.

A complete and precise assessment of the AR properties, should go beyond the values of R_{tot} and T_{tot} and include also the angular dependence of the reflected intensity, polarization properties, as well as a precise discrimination between light diffusion and specular reflectance. Improved performances with respect to the bare SiGe islands are obtained for all the samples when covered with conformal single or double layers made of Si_3N_4 and SiO_2[15] (Tables I and II). Samples I-A, -B -C and III-A, -B and -C were optimized for below band-gap frequencies: the total reflectance remains between 7% and 20% (Fig.4 a)) whereas it varied between 25% and 35% for the bare samples (Fig.2 b)). The different thickness of the conformal Si_3N_4 coatings allows for a slight tuning of the minimum of R_{tot} (e.g. from ∼1500 nm for sample I-C up to ∼2000 nm for sample I-A). For sample III a more pronounced dip in R_{tot} is observed in a narrower spectral range (up to 7%) owing to the presence of larger particles on sample III with respect to sample I (Fig.1 b)).

TABLE II. Values of $< R_{tot} >$ for above band-gap frequencies (AB: 300-1050 nm) and for the full investigated range (AB + BB: 300-2500 nm), $< T_{tot} >$ and $< A_{tot} >$=$< 1 - T_{tot} - R_{tot} >$ (absorbed light) for below band-gap frequencies (BB: 1200-2500 nm), are reported for all the investigated SiGe-based samples. Same quantities are calculated via transfer matrix method for two flat interferential double layers optimized for above band-gap frequencies (2D AB: 65 nm SiO_2 on 65 nm Si_3N_4) and for the full investigated range (2D AB + BB: 145 nm SiO_2 on 145 nm Si_3N_4). The values relative to our random metasurfaces are extracted form the experimental data whereas those relative to the flat layers are from simulations as shown in Fig.SI. 6 and 7.

Range	AB	AB + BB	BB	BB
	$< R_{tot} >$	$< R_{tot} >$	$< T_{tot} >$	$< A_{tot} >$
I	22.0	21.9	56.3	13.9
I-A	10.5	12.4	77.7	9.1
I-B	10.2	13.1	77.7	9.3
I-C	11.4	12.2	77.7	8.2
II	25.0	22.0	53.5	16.4
II-A	12.7	11.0	71.9	13.3
II-B	4.9	10.5	75.0	10.7
II-C	14.1	12.3	71.0	12.0
III	21.8	23.9	54.7	16.3
III-A	8.1	10.3	80.4	8.2
III-B	16.7	14.3	79.0	8.2
III-C	7.7	11.4	79.3	7.4
2D AB	9.7	29.4	58.9	0
2D AB + BB	16.7	26.5	67.6	0

Remarkably, when taking into account the full investigated spectral range spanning from visible to near-infrared frequencies, these metasurfaces outperforms conventional flat ARs (SI Fig.SI. 6 d), f) and j)). While the best double layer coating features an average R_{tot} of about 26%, our samples are in the 8-13% range. A summary of this investigation is shown in Table II.

Finally, as for the bare SiGe islands case, we estimate the light trapping for sample III-A, -B and -C (Fig.4 c)). For these samples, covered with a conformal layer and with additional AR on the backside, T_{tot} is in the range of 60%-80% and it is enhanced with respect to the bare SiGe islands (Fig.2 c)). T_{tot} + R_{tot} increases monotonically providing a light trapping of about 20% at 1200 nm up to negligible values at 2500 nm (see also Table II). Thus, in spite of a better performance in terms of R_{tot} owing to the layers on the backside of the wafer, at these frequencies, the light trapping is about two times less effective for capped islands with respect to the bare case (Fig.2 c) top panel and Fig.4 c)). This is an important observation in view of the exploitation of these structures for specific applications where light trapping should be enhanced with respect

to transparency.

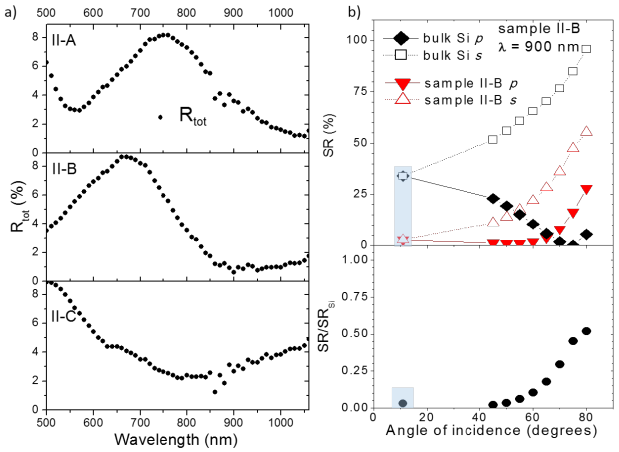


FIG. 5. *Above band-gap anti-reflection coating: sample II-A, -B and -C.* a) From the top to the bottom panel: total reflectance R_{tot} at quasi-normal incidence for samples II-A, II-B and II-C. b) Top panel: specular reflectance SR for *s*- (open symbols) and *p*-polarized (full symbols) incident beam for sample II-B (triangles) and Si wafer (squares). SR for a beam incident on the sample surface at angles larger than 45 degrees is measured with an ellipsometer. SR at 11 degrees (shaded) is obtained from R_{tot} in graph a) and it thus also contains the reflected scattering (R_{tot} = SR + RD, see also Fig.4). Thus it represents an overestimation of SR. Bottom panel: Specular reflectance SR at 900 nm for sample II-B as a function of the incidence angle normalized to SR of Si wafer at the same wavelength. The error in the measured light intensity is less than 1%.

Samples II-A, II-B and II-C were optimized as AR for frequencies above the Si band-gap (table I and Fig.5). For all these samples, R_{tot} can reach values as small as a few % accounting for the good performances of the AR coating. A tuning of the minimum of R_{tot} is possible thank to the different thicknesses of the additional conformal coatings. This leads to a shift in the minimum of R_{tot} from about 850 nm for sample II-C up to 1050 nm for sample II-A. Thus, also in this narrower spectral range, the effect of the additional conformal layers deposited atop the SiGe islands is to improve the AR properties of a factor of two or more with respect to bare islands. Furthermore, at normal incidence, sample II-B is more than a factor of two more performing than a double layer composed of SiO_2 on Si_3N_4 (SI Fig.SI. 7 and Table II).

Angle-resolved measurements of the specular reflectance SR are collected with an ellipsometer (thus disregarding the reflected scattering RD, Fig.5 b)). Averaging the specular reflectance for *s* and *p* polarizations and normalizing this value to that one measured on a Si wafer allows to observe an excellent AR performance up to about 55 degrees (Fig.5 b) bottom panel).

In order to address the composition of the reflected light in terms of scattered and specular reflection we take into account the case of sample II-B for above band-gap frequencies. The reflected scattering (RD, defined as the total reflection minus the specular reflection: RD = R_{tot} - SR) at quasi-normal incidence and integrated over the half solid angle is compared to the corresponding value of R_{tot} (Fig.6 a)). The similar values and spectral features of R_{tot} and RD allow us to conclude that most of the reflected light can be ascribed to the resonant backscattering from the SiGe Mie resonators distributed over the half solid angle atop the sample. The difference between R_{tot} and RD represents the specular reflectance SR and seems to play a minor role.

In order to better assess the composition and features of R_{tot} we characterized SR and RD at different incidence and collection angles by measuring the spectrally- and angularly-resolved bidirectional reflectance distribution function (BRDF)[69,70] (see also SI Fig.SI. 8). Here the incident beam and the detector are scanned along the same meridian and all the measured intensities are normalized to a Lambertian reference (the setup is shown in Fig.6 b)).

Spectrally-integrated measurements show that the BRDF is composed by two distinct parts: a low-intensity, broad pedestal and a sharp peak which correspond to the scattered part RD and the specular reflection SR. The scattering RD (from 0.02 sr^{-1} to 0.06 sr^{-1}, Fig.4 b)) is about 2-3 times lower than that of bare SiGe islands on sample II(RD from 0.06 sr^{-1} to 0.1 sr^{-1}, see also Fig.SI.8 a).

In a small cone (about 10 degrees), the specular reflection is about 2 order of magnitudes larger than the scattering and stays rather constant up to ∼50 degrees, in agreement with Fig.5 b). For excitation beams at angles larger than ∼40 degrees, a slightly enhanced backscattering can be observed (highlighted by an arrow in the inset of Fig.4 c)).

By taking into account the case of excitation at 10 degrees for sample II-B, it is possible to compare this result with those obtained with the spectrophotometer for the same sample (Fig.5 a), central panel) discriminating and quantifying SR and RD independently. Owing to the randomized position and size of the Mie resonators on our samples, the BRDF is invariant for revolutions around the vertical direction (SI Fig.SI. 8 d)). Thus, it is possible to integrate the scattered part over the half solid angle and the specular part over a small solid angle of about ±5 degrees around its maximum, for both angular coordinates. From this analysis, we deduce that the SR is only a few % of R_{tot}, confirming the result previously shown in Fig.5 a) for the integrated R_{tot} and RD.

Finally, the spectrally-resolved BRDF for sample II-B is measured for 3 different directions of the incident beam, θ_{exc} = 0, +45 and +75 degrees (Fig.4 d)) whereas the detection is scanned from -80 to +80 degrees. From the full datasets, we select spectra at quasi-specular, quasi-collinear, quasi-vertical direction and large angles (Fig.6 e)). For all the incident angles, the BRDF features higher values at shorter wavelengths. For nearly-specular detection, the BRDF is larger in all the investigated wavelength range and shows a marked increase at shorter wavelengths. Remarkably, for wavelengths larger than 600 nm the spectral and angular features are rather flat.

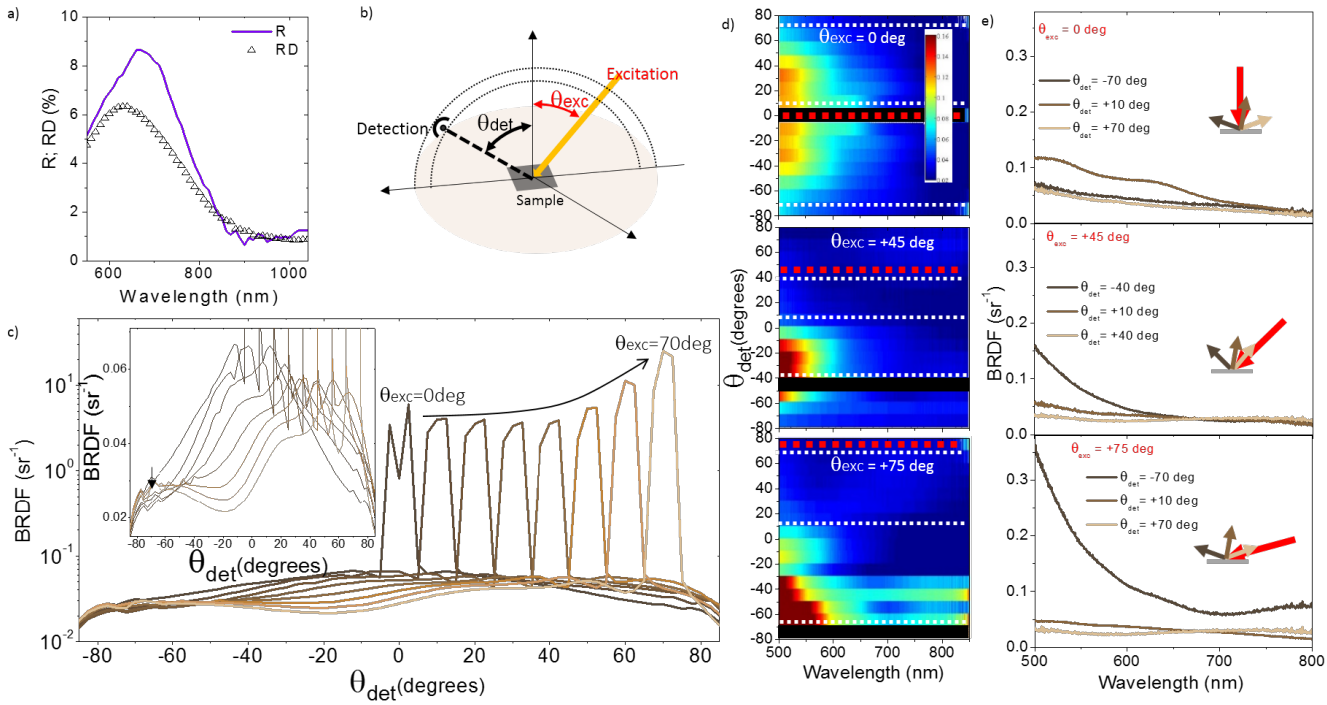


FIG. 6. *Comparison between reflected scattering (RD) and specular reflectance (SR) for sample II-B.* a) Reflected scattering RD (black triangles) and R_{tot} (violet line) for sample II-B at quasi-normal incidence and integrated over the half solid angle atop the sample. b) Sketch of the experimental setup (diffusometer) used for detecting the bidirectional reflectance distribution function (BRDF). The angle of incidence of the excitation (θ_{exc}) and that of the detection (θ_{det}) can be scanned independently over the half solid angle on the same meridian. c) BRDF integrated from 400 nm to 800 nm for sample II-B measured for θ_{exc} from 0 to -70 degrees with respect to the normal to the sample surface and θ_{det} moving from -70 to +70. The sharp and intense peak is SR whereas the low-intensity pedestal is RD. Inset: zoom of the broad pedestal ascribed to RD. The black arrow highlights a slight increase of the RD for incident beam at large angles. d) Full dataset of the spectrally-resolved BRDF for sample II-B for θ_{exc} = 0, +45 and +75 degrees (respectively from the top to the bottom panel). Each panel reports the intensity of the BRDF as a color-scale as a function of wavelength and of θ_{det}. The red dashed lines highlight θ_{exc} whereas the white dashed lines highlight the θ_{det} represented in e). The black shaded areas hide the specular reflection. e) Spectrally-resolved BRDF for sample II-B at θ_{exc} = 0, +45 and +75 degrees (respectively from the top to the bottom panel) for θ_{det} = -70, +10, +70 degrees (top panel), -40, +10, +40 (central panel) and -70, +10, +70 (bottom panel). On each panel the inset displays the excitation (red arrow) and collection (brown arrows) geometry.

IV. DISCUSSION

The extensive optical characterization and simulations performed on our random metasurfaces give a precise insight in the redistribution of the impinging light and its enhanced coupling towards the Si substrate. The analysis of the BRDF demonstrates that the large part of the reflected light is scattered over the half solid angle atop the sample (about 95% of R_{tot}) while the intensity of specular reflection is very limited (SI Fig.SI. 3 a)).

Reflectivity and transmission measurements reveal light trapping within the substrate, pointing at the completely different nature of our ARs with respect to conventional flat thin film coatings. In this latter case, R_{tot} is fully ascribed to specular reflection, rendering the coatings less adapted to all the applications where an increased propagation path of the photons in the device is necessary (e.g. for thin-film photovoltaic). The working principle of our samples is similar to of textured surfaces[9,10] with the additional feature of resonances mediating the light coupling. In view of applications of our AR on thin-film photovoltaic cells or light detectors, the merit of our method is to avoid a direct texturing of the Si wafer thus potentially preserving a high carrier mobility and lifetime[16].

The total reflectance in our disordered samples is strongly reduced over a broad band and a broad angle, in agreement with ordered Mie resonators arrays[15,16,18,21]. We observe that, for ordered arrays of Si-based dielectric particles obtained with top-down methods the best reported value of R_{tot} is about 2% for above band-gap frequencies, whereas in the same spectral interval our best device reaches a value of less than 5%. However, for ordered arrays of Si-based Mie resonators a relevant effect reducing the value of R_{tot} is associated to the well-know Rayleigh anomaly[15] (grating effect), whereas in our case all the AR effect can be truly ascribed to the energy channeling mediated by the Mie resonances formed within the SiGe particles. Thus, owing to the randomness of our samples we obtain a flatter spectral shape of R_{tot} with respect to previous reports[15].

In contrast with previous reports which focused only on above band-gap frequencies[15,16,18,19,21], we extended this idea

to below band-gap frequencies in the near-infrared (∼1050-2500 nm) where R_{tot} can be as low as 7%. Moreover we showed the possibility of tuning the minimum of R_{tot} both for below- and above band-gap frequencies by adjusting the thickness of additional conformal layers deposited atop the SiGe islands. In addition, these conformal layers have the function of encapsulating the SiGe islands, rendering the metasurface more robust against mechanical damage and protecting the underlying structures from humidity.

A full assessment of the performances of our spontaneously assembled structures with respect to existing examples of dielectric Mie resonators in the literature should take into account the full range of frequencies addressed here, as well as the light trapping effect and the composition of light in terms of scattered reflection and specular reflection. Unfortunately, these data are not available in the literature and a comparison is not possible, which further accounts for the importance of our findings and characterizations.

In principle, this fabrication method can be performed at relatively low temperature[71] (e.g. at 300 °C for thin, amorphous Ge layers) and it can be used on custom-made arbitrary SiO_2 layers[43,45] relaxing the need of a commercial UT-SOI. Importantly, the duration of the dewetting process does not depend on the sample size, but only on the thickness of the thin Si(Ge) layer and lowering the temperature budget is possible, in spite of a longer annealing time. In principle, this fabrication method offers the possibility to implement efficient AR coatings on existing devices[72] (e.g. photovoltaic cells, C-MOS and CCD cameras, Si- and Ge-based photo detectors).

V. CONCLUSIONS

We showed that joining annealing of this silicon films with epitaxial growth enable the formation of high density SiGe-based islands featuring a large vertical aspect ratio, a large spread of size with a good spatial isotropy of the particles's size distribution. Our method represents a step forward in self-assembly of 3D structures where the size and the density of the particles are usually correlated.

The performances of our device can be adapted and improved employing an optimized *ad hoc* buried oxide[43,45,64] and targeting specific wavelengths ranges with an appropriate choice of particles size. These possibilities bring the additional advantage of relaxing the need for expensive commercial UT-SOI[43,45] opening up the use of this method on other substrates (e.g. glass, Ge, SiC).

The strengths of this method are manifold: I) the duration of the process does not depend on the extension of the wafer but only on the composition and thickness of the top thin layer; II) dewetting can be exploited at relatively low temperature[71] and thus it can be compatible with back-end processing of C-MOS circuitry[72]; III) it is a lithography-free approach avoiding multiple, polluting, chemical cleaning steps as it relies only on deposition and annealing; IV) it provides efficient AR in extremely broad ranges of frequencies exceeding those shown so far for similar systems[15,16,18,19,21].

FUNDING INFORMATION

This project has received funding from the European Unions Horizon 2020 research and innovation programme under grant agreement no. 654148 Laserlab-Europe. We also acknowledge the Projects PHC MAGHREB (No. 32595SL), EMMAG-Erasmus Mundus Maghreb and Egypt, the PRCI network ULYSSES (ANR-15-CE24-0027-01) funded by the French ANR agency, the LASER-LAB Europe project ARES financed by the EU, the SATT-Sud Est Project PROMETHEUS, the A*MIDEX Project (No. ANR-11-IDEX-0001-02) funded by the Investissements d'Avenir, a French Government program managed by the French National Research Agency (ANR).

ACKNOWLEDGMENTS

The authors thank the Nanotecmat Platform of the IM2NP Institute of Marseille and the CP2M and CINaM microscopy centers of Aix-Marseille University.

† Corresponding author: checcucci@lens.unifi.it
‡ Corresponding author: thomas.wood@ec-lyon.fr
⁕ Corresponding author: marco.abbarchi@im2np.fr
* Present address: Institut de Nanotechnologies de Lyon, Ecole Centrale de Lyon, CNRS (UMR 5270), 69134 Ecully, France
** Present address: GREMAN LAB/ST Microelectronics 16 Rue Pierre et Marie Curie 37071 Tours, France.

[1] S. Chattopadhyay, Y. Huang, Y.-J. Jen, A. Ganguly, K. Chen, and L. Chen, Materials Science and Engineering: R: Reports **69**, 1 (2010).
[2] H. K. Raut, V. A. Ganesh, A. S. Nair, and S. Ramakrishna, Energy & Environmental Science **4**, 3779 (2011).
[3] M. L. Brongersma, Y. Cui, and S. Fan, Nature materials **13**, 451 (2014).
[4] I.-S. Yu, Y.-W. Wang, H.-E. Cheng, Z.-P. Yang, and C.-T. Lin, International Journal of Photoenergy **2013** (2013).
[5] K. Kim, G. Y. Song, Y. T. Kim, J. H. Moon, and J. Heo, Surface and Coatings Technology (2017).
[6] E. Yablonovitch and G. D. Cody, IEEE Transactions on Electron Devices **29**, 300 (1982).
[7] L. Escoubas, J. Simon, M. Loli, G. Berginc, F. Flory, and H. Giovannini, Optics communications **226**, 81 (2003).
[8] Y.-F. Huang, S. Chattopadhyay, Y.-J. Jen, C.-Y. Peng, T.-A. Liu, Y.-K. Hsu, C.-L. Pan, H.-C. Lo, C.-H. Hsu, Y.-H. Chang, *et al.*, Nature nanotechnology **2**, 770 (2007).
[9] X. Sheng, S. G. Johnson, J. Michel, and L. C. Kimerling, Optics Express **19**, A841 (2011).
[10] V. Ganapati, O. D. Miller, and E. Yablonovitch, IEEE Journal of Photovoltaics **4**, 175 (2014).

[11] J. Yang, F. Luo, T. S. Kao, X. Li, G. W. Ho, J. Teng, X. Luo, and M. Hong, Light: Science & Applications **3**, e185 (2014).
[12] H. A. Atwater and A. Polman, Nature materials **9**, 205 (2010).
[13] R. H. Siddique, J. Mertens, H. Hölscher, and S. Vignolini, (2017).
[14] N. Odebo Lank, R. Verre, P. Johansson, and M. Kall, Nano Letters **17**, 3054 (2017).
[15] P. Spinelli, M. Verschuuren, and A. Polman, Nature Communications **3**, 692 (2012).
[16] P. Spinelli, B. Macco, M. Verschuuren, W. Kessels, and A. Polman, Applied Physics Letters **102**, 233902 (2013).
[17] N. Fofang, T. Luk, M. Okandan, G. Nielson, and I. Brener, Optics express **21**, 4774 (2013).
[18] J. Proust, A.-L. Fehrembach, F. Bedu, I. Ozerov, and N. Bonod, Scientific reports **6**, 24947 (2016).
[19] J. Choi, T. S. Lee, D. S. Jeong, W. S. Lee, W. M. Kim, K.-S. Lee, D. Kim, and I. Kim, Journal of Physics D: Applied Physics **49**, 375108 (2016).
[20] V. E. Babicheva, M. I. Petrov, K. V. Baryshnikova, and P. A. Belov, JOSA B **34**, D18 (2017).
[21] T. Bottein, T. Wood, T. David, J. B. Claude, L. Favre, I. Berbézier, A. Ronda, M. Abbarchi, and D. Grosso, Advanced Functional Materials **27** (2017).
[22] J. A. Schuller, R. Zia, T. Taubner, and M. L. Brongersma, Physical review letters **99**, 107401 (2007).
[23] Q. Zhao, J. Zhou, F. Zhang, and D. Lippens, Materials Today **12**, 60 (2009).
[24] A. B. Evlyukhin, C. Reinhardt, A. Seidel, B. S. Luk'yanchuk, and B. N. Chichkov, Physical Review B: Condensed Matter and Materials Physics **82**, 045404 (2010).
[25] A. B. Evlyukhin, S. M. Novikov, U. Zywietz, R. L. Eriksen, C. Reinhardt, S. I. Bozhevolnyi, and B. N. Chichkov, Nano letters **12**, 3749 (2012).
[26] A. B. Evlyukhin, C. Reinhardt, E. Evlyukhin, and B. N. Chichkov, JOSA B **30**, 2589 (2013).
[27] D. Lin, P. Fan, E. Hasman, and M. L. Brongersma, science **345**, 298 (2014).
[28] S. Jahani and Z. Jacob, Nature nanotechnology **11**, 23 (2016).
[29] X. Li, J. Gao, L. Xue, and Y. Han, Advanced Functional Materials **20**, 259 (2010).
[30] K. Vynck, M. Burresi, F. Riboli, and D. S. Wiersma, Nature materials **11**, 1017 (2012).
[31] M. Burresi, F. Pratesi, K. Vynck, M. Prasciolu, M. Tormen, and D. S. Wiersma, Optics express **21**, A268 (2013).
[32] C. Rockstuhl and T. Scharf, *Amorphous nanophotonics* (Springer Science & Business Media, 2013).
[33] H. Yasuda, R. Matsuno, N. Koito, H. Hosoda, T. Tani, and M. Naya, Applied Physics Letters **111**, 231105 (2017).
[34] Y. Wu, J. D. Fowlkes, and P. D. Rack, Journal of Materials Research **26**, 277 (2011).
[35] S. Hong, T. Kang, D. Choi, Y. Choi, and L. P. Lee, ACS nano **6**, 5803 (2012).
[36] A. B. Tesler, B. M. Maoz, Y. Feldman, A. Vaskevich, and I. Rubinstein, The Journal of Physical Chemistry C **117**, 11337 (2013).
[37] S. Morawiec, M. J. Mendes, S. Mirabella, F. Simone, F. Priolo, and I. Crupi, Nanotechnology **24**, 265601 (2013).
[38] F. Bisio, R. Proietti Zaccaria, R. Moroni, G. Maidecchi, A. Alabastri, G. Gonella, A. Giglia, L. Andolfi, S. Nannarone, L. Mattera, *et al.*, ACS nano **8**, 9239 (2014).
[39] S. V. Makarov, V. A. Milichko, I. S. Mukhin, I. I. Shishkin, D. A. Zuev, A. M. Mozharov, A. E. Krasnok, and P. A. Belov, Laser & Photonics Reviews **10**, 91 (2016).
[40] R. Yu, P. Mazumder, N. F. Borrelli, A. Carrilero, D. S. Ghosh, R. A. Maniyara, D. Baker, F. J. Garcia de Abajo, and V. Pruneri, ACS Photonics **3**, 1194 (2016).
[41] S. Kunwar, M. Sui, Q. Zhang, P. Pandey, M.-Y. Li, and J. Lee, Nano-Micro Letters **9**, 17 (2017).
[42] M. Abbarchi, M. Naffouti, B. Vial, A. Benkouider, L. Lermusiaux, L. Favre, A. Ronda, S. Bidault, I. Berbezier, and N. Bonod, ACS nano **8**, 11181 (2014).
[43] M. Naffouti, T. David, A. Benkouider, L. Favre, A. Ronda, I. Berbezier, S. Bidault, N. Bonod, and M. Abbarchi, Nanoscale **8**, 7768 (2016).
[44] M. Naffouti, T. David, A. Benkouider, L. Favre, M. Cabie, A. Ronda, I. Berbezier, and M. Abbarchi, Nanotechnology **27**, 305602 (2016).
[45] T. Wood, M. Naffouti, J. Berthelot, T. David, J.-B. Claude, L. Metayer, A. Delobbe, L. Favre, A. Ronda, I. Berbezier, N. Bonod, and M. Abbarchi, ACS Photonics **4**, 873 (2017).
[46] M. Naffouti, R. Backofen, M. Salvalaglio, T. Bottein, M. Lodari, A. Voigt, T. David, A. Benkouider, I. Fraj, L. Favre, *et al.*, Science Advances **3**, eaao1472 (2017).
[47] D. Srolovitz and S. Safran, Journal of Applied Physics **60**, 247 (1986).
[48] D. Srolovitz and S. Safran, Journal of applied physics **60**, 255 (1986).
[49] E. Jiran and C. Thompson, Journal of electronic materials **19**, 1153 (1990).
[50] D. T. Danielson, D. K. Sparacin, J. Michel, and L. C. Kimerling, Journal of applied physics **100**, 083507 (2006).
[51] C. M. Müller and R. Spolenak, Acta materialia **58**, 6035 (2010).
[52] F. Cheynis, E. Bussmann, F. Leroy, T. Passanante, and P. Müller, Physical Review B **84**, 245439 (2011).
[53] C. V. Thompson, Annual Review of Materials Research **42**, 399 (2012).
[54] F. Leroy, F. Cheynis, T. Passanante, and P. Müller, Physical Review B **85**, 195414 (2012).
[55] G. Hyun Kim, R. V. Zucker, J. Ye, W. Craig Carter, and C. V. Thompson, Journal of Applied Physics **113**, 043512 (2013).
[56] R. V. Zucker, G. H. Kim, W. C. Carter, and C. V. Thompson, Comptes Rendus Physique **14**, 564 (2013).
[57] G. Boussinot and E. A. Brener, Physical Review E **92**, 032408 (2015).
[58] R. V. Zucker, G. H. Kim, J. Ye, W. C. Carter, and C. V. Thompson, Journal of Applied Physics **119**, 125306 (2016).
[59] M. Aouassa, I. Berbezier, L. Favre, A. Ronda, M. Bollani, R. Sordan, A. Delobbe, and P. Sudraud, Applied Physics Letters **101**, 013117 (2012).
[60] E. Sutter and P. Sutter, Nanotechnology **17**, 3724 (2006).
[61] M. Naffouti, T. David, A. Benkouider, L. Favre, A. Delobbe, A. Ronda, I. Berbezier, and M. Abbarchi, Small **12**, 6115 (2016).
[62] M. Aouassa, L. Favre, A. Ronda, H. Maaref, and I. Berbezier, New Journal of Physics **14**, 063038 (2012).
[63] P. Zhang, B. Yang, P. Rugheimer, M. Roberts, D. Savage, F. Liu, and M. Lagally, Journal of Physics D: Applied Physics **42**, 175309 (2009).
[64] J. van de Groep and A. Polman, Optics express **21**, 26285 (2013).
[65] H. Kallel, A. Chehaidar, A. Arbouet, and V. Paillard, Journal of Applied Physics **114**, 224312 (2013).
[66] A. Chehaidar and H. Jdidi, International Journal of Nanotechnology **12**, 663 (2015).
[67] H. Kallel, A. Arbouet, G. BenAssayag, A. Chehaidar, A. Potié, B. Salem, T. Baron, and V. Paillard, Physical Review B **86**, 085318 (2012).
[68] X. Zhu, W. Yan, U. Levy, N. A. Mortensen, and A. Kristensen, Science Advances **3**, e1602487 (2017).
[69] W. Matusik, H. Pfister, M. Brand, and L. McMillan, (2003).
[70] T. A. Germer, J. C. Stover, and S. Schroeder, Spectrophotometry: Accurate Measurements of the Optical Properties of Materials

(2014).

[71] Y. Wakayama, T. Tagami, and S.-i. Tanaka, Thin Solid Films **350**, 300 (1999).

[72] Y. H. D. Lee and M. Lipson, IEEE Journal of Selected Topics in Quantum Electronics **19**, 8200207 (2013).